



A regularized deconvolution model for sub-grid dispersion in large eddy simulation of turbulent spray flames

Qing Wang^a, Xinyu Zhao^{b,*}, Matthias Ihme^a

^a Department of Mechanical Engineering, Stanford University, Stanford CA, United States

^b Department of Mechanical Engineering, University of Connecticut, Storrs CT, United States

ARTICLE INFO

Article history:

Received 27 December 2018

Revised 19 May 2019

Accepted 19 May 2019

Keywords:

Large-eddy simulation

Spray combustion

Sub-grid dispersion

Deconvolution

ABSTRACT

In this study, a sub-grid scale (SGS) dispersion model is developed for simulating turbulent spray flames. This model employs a regularized deconvolution method (RDM) to determine the sub-grid fluctuations from the filtered velocity field. The model is examined in simulations of a turbulent counterflow n-dodecane spray flame, and benchmarked against a simplified Langevin model (SLM) and simulations without dispersion closure (NOM). To identify conditions that characterize the importance of the spray-flame coupling, a regime diagram is constructed from physical arguments and theoretical analysis by considering idealized conditions. Based on the proposed criteria, a range of operating conditions is considered, involving different Stokes- and Reynolds numbers as well as inert and reacting conditions. *A priori* DNS analyses are performed to compare the probability density functions (PDFs) of slip velocities. Significant discrepancies between models are observed for smaller Stokes numbers. Subsequently, large eddy simulations (LES) are performed and effects of mesh resolution on statistical flow-field quantities are investigated. Qualitative and quantitative differences are observed for coarse-grid simulations with larger droplets, where a double-flame structure is predicted by DNS and LES-RDM, whereas a single flame is predicted by LES-NOM and LES-SLM. For the finer grid, all three LES models predict the double-flame structure. Turbulence modulation by the spray is expected to play a role in creating different flame topologies, and the RDM-based SGS-closure model is shown to provide improved predictions for the dispersed and carrier phases for a wider range of grid resolution.

© 2019 The Combustion Institute. Published by Elsevier Inc. All rights reserved.

1. Introduction

Industrial processes often involve turbulent multiphase flows, as seen in internal and aeronautical combustion engines, fluidized bed reactors, pulverized coal combustion, and solid particles in solar receivers. Turbulent dispersion of droplets and particles can be considered as a manifestation of the turbulence-scalar interactions that are present in such flows, among other mechanisms such as turbulence-chemistry and turbulence-radiation interactions. Similar to closure problems frequently encountered in turbulent combustion systems, sub-grid interactions between turbulence, droplet dispersion, evaporation, and heat transfer processes require consideration, in the context of Reynolds Averaged Navier–Stokes (RANS) simulations and large eddy simulations (LES) [1]. Closure models for turbulence dispersion can determine the location and evaporation rates of droplets and, subsequently, influence the mixing, ignition and combustion processes.

The dispersion of droplets and particles due to turbulence is usually modeled using stochastic models in the context of an Eulerian–Lagrangian formulation. For various turbulent dispersion models, the time history of the carrier fluid velocity experienced by the dispersed phase requires specification. Over the past decades, significant progress has been made on the development of sub-grid turbulence dispersion models [1–11]. Studies were performed for droplets in homogeneous isotropic turbulent non-reacting flows [12]. Two approaches were proposed to approximate the instantaneous carrier fluid velocity field. One approach is a random walk model, in which the instantaneous velocity is represented as the sum of the local mean (or LES-filtered) velocity obtained from the carrier phase and a random fluctuating velocity, generated from a Gaussian distribution with zero mean and a variance related to the turbulent velocity scale. This approach has been widely employed in spray simulations in the RANS context. When used in LES, it has been shown that particle statistics obtained using the random walk model are quite similar to those obtained without any dispersion models [12].

Another approach is to employ a Lagrangian stochastic differential equation (SDE) to compute the instantaneous “seen” velocity

* Corresponding author.

E-mail address: xinyu.zhao@uconn.edu (X. Zhao).

directly. This approach usually relies on the assumption of certain stochastic diffusion processes [1,13–15]. The SDE-based dispersion models were found to behave better than the random walk models in inhomogeneous flows [13] in RANS, and they also consistently perform better in *a-priori* LES evaluation, in predicting the particle kinetic energy and invariance with different filter sizes [12]. With respect to LES applications, deconvolution based models have been proposed in the literature [9,12]. There, the approximate deconvolution method is used to improve the prediction near the cutoff scale, thereby recovering more kinetic energy of the subgrid level.

Adapting the models to inhomogeneous reacting environments requires further study. Practical devices, such as aeronautical combustors, are almost never homogeneous or isotropic. With the compact design of modern combustors, spray droplets have greater probability to interact with flames, as demonstrated by existing device-scale simulations [16]. It is unclear how existing turbulent dispersion models extend to inhomogeneous and anisotropic flows with density variations. More importantly, it is also unclear how the presence of flames affects the performance of different models that were derived for homogeneous and isotropic non-reacting flows. Therefore, the objective of this work is to study the influence of various thermophysical environments on the droplet dynamics and to assess the performance of turbulence dispersion models. To this end, DNS and LES are employed to examine the performance of sub-grid dispersion models in the presence of combustion. Analysis of DNS-data enables the decoupling of various modeling aspects, thereby facilitating the direct assessment of the impact of individual sub-models.

The configuration under investigation is a three-dimensional monodispersed turbulent counterflow spray flame, where bifurcating flame behavior was reported for different droplet diameters [17]. Two models are examined, including a stochastic closure and a deconvolution closure that is developed in this study. The modeling results are subsequently compared against results obtained from LES calculations that are performed without a dispersion model. In this study, we limit the model development and discussions to conditions where droplet-droplet interactions are negligible, the point-particle assumption is adequate and isolated droplet combustion is neglected [18]. An Eulerian–Lagrangian framework is adopted to describe the two-phase flow. It should be noted that the models developed in this study are also applicable to solid particles under the same assumptions.

The remainder of this paper is structured as follows. The modeling framework and governing equations for carrier and dispersed phases are introduced in Section 2, including details of the sub-grid dispersion models. A theoretical analysis is then developed in Section 3 to identify conditions under which flame-droplet interactions become significant, providing a physical foundation for the selection of the test cases. In Section 4, the flame configuration under consideration is detailed, and the computational setup is discussed. Section 5 first quantifies the numerical conditions that require the consideration of sub-grid turbulent dispersion effects. *A posteriori* simulations are then conducted to examine the performances of various submodels in accounting for the dynamic interactions between turbulence, heat transfer, and mass exchange. Finally, conclusions and suggestions for future work are offered in Section 6.

2. Governing equations and model formulation

2.1. Governing equations for the gas phase

In the present work, an Eulerian–Lagrangian framework is adopted for simulating turbulent spray combustion. Two-way coupling is considered and droplet-droplet interactions are neglected because of the low mass-loading ratio considered as shown

in Section 4. In the present work, a low-Mach-number formulation is adopted, in which density and thermo-chemical states are evaluated from a combustion model. The governing equations describing the conservation of mass and momentum in the gas phase take the following form [19]:

$$\partial_t \bar{\rho} + \nabla \cdot (\bar{\rho} \tilde{\mathbf{u}}) = -\langle d_t(m_d) \rangle, \quad (1a)$$

$$\partial_t (\bar{\rho} \tilde{\mathbf{u}}) + \nabla \cdot (\bar{\rho} \tilde{\mathbf{u}} \otimes \tilde{\mathbf{u}}) = -\nabla P + \nabla \cdot (\bar{\boldsymbol{\tau}} + \boldsymbol{\tau}_t) - \langle d_t(m_d \mathbf{u}_d) \rangle, \quad (1b)$$

where \mathbf{u} and \mathbf{u}_d are the velocity vectors for the carrier phase and dispersed phase, respectively, P is the hydrodynamic pressure, and m_d is the droplet mass; $\bar{\boldsymbol{\tau}}$ is the filtered viscous stress tensor and $\boldsymbol{\tau}_t$ is the sub-grid scale stress tensor that is modeled by a dynamic Smagorinsky procedure [20]. $\langle \phi \rangle = (1/V_{\text{cell}}) \sum_{i=1}^{V_{\text{cell}}} \phi_i$ denotes the volume average of ϕ over each computational cell.

To examine the effect of spray dispersion model on combustion, we consider a flamelet-progress variable (FPV) combustion model to represent the gas-phase combustion [21]. In this model, transport equations for mixture fraction Z and progress variable C [22] are solved in conjunction with Eq. (1). The turbulence-flame interaction for the FPV model is represented by a presumed probability density function (PDF) model, in which the reaction source term for C is computed as

$$\tilde{\omega}_C = \int \int \dot{\omega}_C(Z, C) P(C|Z) \tilde{P}(Z) dZ dC. \quad (2)$$

In Eq. (2), $P(C|Z)$ is the PDF of the progress variable conditioned on the mixture fraction, which is modeled by a δ -PDF. $\tilde{P}(Z)$ is the PDF of the mixture fraction that is modeled by a β -PDF to account for sub-grid scale fluctuations in turbulent flows. The closure of $\tilde{P}(Z)$ requires knowledge of the mixture fraction variance, \tilde{Z}''^2 , which is obtained from a transport equation. With this, the transport equations required by the FPV approach are given as follows:

$$\partial_t (\bar{\rho} \tilde{Z}) + \nabla \cdot (\bar{\rho} \tilde{\mathbf{u}} \tilde{Z}) = -\nabla \cdot (\bar{\mathbf{J}}_Z + \mathbf{J}_{Z,t}) - \langle \dot{m}_d \rangle, \quad (3a)$$

$$\partial_t (\bar{\rho} \tilde{C}) + \nabla \cdot (\bar{\rho} \tilde{\mathbf{u}} \tilde{C}) = -\nabla \cdot (\bar{\mathbf{J}}_C + \mathbf{J}_{C,t}) + \bar{\rho} \tilde{\omega}_C, \quad (3b)$$

$$\partial_t (\bar{\rho} \tilde{Z}''^2) + \nabla \cdot (\bar{\rho} \tilde{\mathbf{u}} \tilde{Z}''^2) = -\nabla \cdot (\bar{\mathbf{J}}_{Z''^2} + \mathbf{J}_{Z''^2,t}) + \bar{\rho} \tilde{q}_{Z''^2} + S_{Z''^2}, \quad (3c)$$

where $\tilde{q}_{Z''^2}$ is the production term [23], and $S_{Z''^2} = \langle \dot{m}_d \rangle (1 - 2\tilde{Z})(\tilde{Z}''^2/\tilde{Z})$ is the source term arising from the droplet evaporation. The chemical source term and thermochemical transport properties are tabulated and parameterized by \tilde{Z} , \tilde{C} , and \tilde{Z}''^2 . The last terms on the right-hand sides of Eqs. (1), (3a) and (3c) account for the momentum and mass transfer from the dispersed phase to the carrier phase, the details of which will be discussed in Section 2.2.

To describe the reaction chemistry of n-dodecane, a 24-species reduced mechanism [17] is employed. The FPV chemistry table is constructed from one-dimensional counterflow diffusion flame simulations traversing the S-shape curve. In this approach, the liquid fuel is assumed to be pre-vaporized, and evaporation is considered by reducing the temperature of the fuel stream by an amount that corresponds to the latent heat of evaporation in the one-dimensional flamelet computations. It should be noted that the FPV model has limitation in capturing all salient features of spray combustion, and models of higher fidelity are needed if robust prediction of spray flames is required [24–28]. In this study, we use this simplified approach since this work is primarily concerned with the analysis of different sub-grid dispersion models.

2.2. Governing equations for the dispersed phase

The dispersed phase is modeled with a Lagrangian approach using the following equations [29]:

$$\frac{dm_d}{dt} = -\frac{Sh_g m_d}{3Sc_g \tau_p} \ln(1 + B_m), \quad (4a)$$

$$\frac{d\mathbf{u}_d}{dt} = \frac{f_1}{\tau_p} (\mathbf{u}^+ - \mathbf{u}_d), \quad (4b)$$

$$\frac{dT_d}{dt} = \frac{f_2}{\tau_p} \frac{Nu_g c_{p,m}}{3Pr_g c_l} (T^+ - T_d) + \frac{L_v}{m_d c_l} \frac{dm_d}{dt}, \quad (4c)$$

where $B_m = (Y_{f,S} - Y_{f,v}) / (1 - Y_{f,S})$ is the Spalding mass transfer number of the fuel, $c_{p,m} = (1 - Y_v)c_{p,g} + Y_v c_{p,v}$ is the heat capacity of the gas mixture, c_l is the heat capacity of the droplet, τ_p is the particle relaxation time, and \mathbf{u}^+ and T^+ are the carrier-phase velocity and temperature seen by the droplets, respectively. f_1 and f_2 are the correction functions [29] that account for the drag force and the convective heat transfer, respectively. An equilibrium evaporation model is used, where $Sh_g = 2 + 0.6Re_d^{1/2} Sc_g^{1/3}$ and Sc_g denote the Sherwood and Schmidt numbers [30], respectively, and Re_d is the slip Reynolds number. The latent heat is represented by L_v . Nu_g and Pr_g are the Nusselt and Prandtl numbers, respectively. In these expressions, subscripts g , d , and v denote the gas-phase, dispersed phase, and vapor phase, respectively, and the subscript S refers to conditions at the droplet surface. The source terms in the carrier-phase equations arising from the droplet dynamics are evaluated using a particle-source-in-cell method [31]. In the present study, one droplet per parcel is specified. Therefore, each individual droplet is tracked and accounted for through Eq. (4).

If the turbulent flow field of the carrier phase is fully resolved, \mathbf{u}^+ and T^+ in Eqs. (4b) and (4c) are essentially the instantaneous velocity and temperature fields, interpolated to the droplet location. However, for LES or RANS, the interpolation of the grid velocity does not provide the instantaneous flow field that is seen by the dispersed phase. Therefore, modeling is required to account for the influence of sub-grid velocity fluctuations in the drag model (i.e., termed turbulent dispersion models) and in the heat transfer models. Details of the sub-grid dispersion closures are discussed next, including a deconvolution model that is applicable to both velocity and scalars, and a stochastic dispersion model.

2.3. Regularized deconvolution model for sub-grid dispersion

The regularized deconvolution method is formulated here to model the velocity \mathbf{u}^+ and T^+ in Eqs. (4b) and (4c) [32]. This method reconstructs the sub-grid fluctuations of the flow field, hence can capture the interactions between droplets and flow structures that are smaller than the mesh size.

In LES, the filter operation is imposed implicitly by the discretization scheme, and $\tilde{\phi}$ is the variable solved from the governing equations. In the present study, the 1-D filter operation as specified in Eq. (5) is performed sequentially for each direction. On a structured mesh in each direction, the filter G takes the form of a top-hat filter with the filter width Δ_i being the grid spacing at node i :

$$G(x, x_i; \Delta_i) = \begin{cases} 1/\Delta_i, & \text{if } |x - x_i| \leq \Delta_i/2; \\ 0, & \text{otherwise.} \end{cases} \quad (5)$$

To represent sub-grid structures, a sub-grid mesh of size N^* with grid spacing Δ^* is introduced where additional data points are added between grid points in the primary LES mesh of size N . This is illustrated in Fig. 1. Define the stencil for node i as $S_i =$

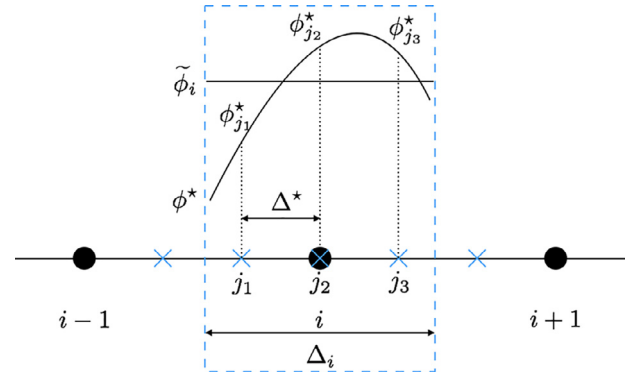


Fig. 1. Illustration of the LES grid of size Δ and the sub-grid mesh of size Δ^* .

$\{x | |x - x_i| \leq \Delta_i/2\}$. With this definition, there are no overlaps between S_i and its neighboring stencils. Specifically, node i requires information from their immediate neighboring cells only, by the definition of the filter. This provides the advantage that, in the context of multiprocessor computing, no additional communication cost is incurred in the reconstruction process. Information from the ghost cells that is available from boundary condition communications is sufficient to perform the reconstruction. The solution field is interpolated onto the sub-grid mesh, using a spline interpolation due to its capability of employing different boundary conditions. With this, RDM is formulated as a constrained optimization problem that takes the form:

$$\phi^* = \arg \min_{\substack{\underline{c} \phi^* = \tilde{\phi} \\ \phi^- \leq \phi^* \leq \phi^+}} \left(\|P \tilde{\phi} - \underline{G} \phi^*\|_2 + \alpha \|D \phi^*\|_2 \right), \quad (6)$$

where ϕ and the filter kernels are represented in discrete forms, and $\underline{\phi}$ is a vector constructed from ϕ along each direction on the structured mesh. Note that RDM is performed on the sub-grid mesh, as indicated by the blue crosses in Fig. 1. In Eq. (6), $P \in \mathbb{R}^{(N^* \times N)}$ is the interpolation matrix that projects the LES solution from the computational grid of size N to the sub-grid mesh of size N^* , $\underline{G} \in \mathbb{R}^{(N^* \times N^*)}$ is the discrete filter kernel, $\underline{D} \in \mathbb{R}^{(N^* \times N^*)}$ is a matrix constructed for the second order derivative using a finite difference discretization, $\underline{C} \in \mathbb{R}^{(N \times N^*)}$ is the mean-preserving constraint matrix, and α is the regularization factor that is estimated as $\alpha = \text{tr}(\underline{G}^T \underline{G}) / \text{tr}(I)$ [33]. The first argument in the objective function in Eq. (6) is the L_2 -norm of the error between the explicitly filtered deconvolved quantity and the LES solution that is projected onto the sub-grid mesh. Minimization of this L_2 -norm provides a reconstruction of the sub-grid scale structures of ϕ . The second argument in the objective function regularizes the smoothness of the deconvolved scalar field. With this, the differentiation of the deconvolved quantities is well defined. The constraints in Eq. (6) ensure the conservation and boundedness of the deconvolved solution. The conservation is enforced at each stencil through the equality constraint, so that the volume average of the deconvolved solution in a stencil equals the filtered variable at the LES node in that stencil. As illustrated in Fig. 1, the mean of $\phi^*(\mathbf{x})$ for $\mathbf{x} \in S_i$ equals $\tilde{\phi}_i$, which is

$$\tilde{\phi}_i = \frac{1}{V_i} \int_{V_i} \phi^* dV = \sum_{\mathbf{x}_j \in S_i} w(\mathbf{x}_j) \phi_j^* = \underline{C}_i \phi^*, \quad (7)$$

where \underline{C}_i is the i th row of \underline{C} , which is constructed from the weight coefficients $w(\mathbf{x}_j)$ for each stencil. With this condition, the quantity of interest at each node i is conserved locally. For an equidistant

grid, $w(\mathbf{x}_j) = 1/|S_i|$, where $|S_i|$ is the number of nodes in stencil S_i .

The inequality constraints ensure the boundedness of species and temperature, which is not relevant for reconstructing the velocity as there are no physical bounds that are pertinent. Solving Eq. (6) using the Lagrange multiplier method without the inequality constraints provides a deconvolution solution ϕ_0^* in the following form:

$$\underline{\phi}_0^* = \underline{Q} \tilde{\phi}. \quad (8)$$

where $\underline{Q} \in \mathbb{R}^{(n^* \times n)}$ is the first n^* rows of the solution matrix \underline{Q}_0 to Eq. (6), taking the following form:

$$\underline{Q}_0 = \begin{bmatrix} \underline{G}^T \underline{G} + \alpha \underline{D}^T \underline{D} & \underline{C}^T \\ \underline{C} & \underline{0} \end{bmatrix}^{-1} \begin{bmatrix} \underline{G}^T \underline{P} \\ \underline{I} \end{bmatrix}. \quad (9)$$

For sub-grid dispersion models, ϕ_0^* is employed to model the i th component of the “seen” velocity \mathbf{u}^* at droplet location \mathbf{x}_d , i.e.,

$$u_i^+(\mathbf{x}_d) = u_{0,i}^*(\mathbf{x}_d). \quad (10)$$

It should be noted that the information beyond the cutoff scale is only partially recovered by the above deconvolution procedure. To consider the remaining scales, the fluctuation of the reconstructed field can be rescaled by the variance of the variable that is computed from a well-established physical model [34]. A detailed description of this scale-similarity based RDM model is provided in [35], and it is applied to the reconstruction of scalars such as temperature T^+ . To ensure a direct comparison among models, in the following RDM is only applied to the modeling of dispersion in momentum, hence the scale-similarity model is not employed for results shown subsequently.

2.4. Other models for sub-grid dispersion

When no dispersion model is applied, the “seen” velocity is obtained by interpolating the gas-phase velocity $\tilde{\mathbf{u}}$ to each particle location, using a second-order interpolation scheme. The sub-grid gas-phase fluctuation is neglected, which is a reasonable approximation when the LES is well-resolved or when St_K is sufficiently large. However, for variable Stokes numbers that are ubiquitously encountered in spray flames, such conditions cannot always be ensured.

Stochastic models have traditionally been employed in RANS simulations of spray combustion, and this class of closure models is another popular option in LES [1,4–7]. Compared to the pure random walk models, Langevin-based stochastic models were shown to better recover the turbulence statistics in the small Stokes limit [13]. Stochastic fluctuations are added to the interpolated filtered velocity component to account for the sub-grid fluctuation, taking the following form:

$$\mathbf{u}^+(\mathbf{x}_d) = \tilde{\mathbf{u}}(\mathbf{x}_d) + \mathbf{u}_d''(\mathbf{x}_d), \quad (11)$$

where the component of the fluctuating sub-grid velocity vector \mathbf{u}_d'' is obtained as [4]

$$\begin{aligned} & \mathbf{u}_d''(\mathbf{x}_d + \mathbf{u}_d \Delta t, t + \Delta t) - \mathbf{u}_d''(\mathbf{x}_d, t) \\ &= \left[-\mathbf{u}_d'' \cdot \nabla \tilde{\mathbf{u}}(\mathbf{x}_d, t) + \nabla \cdot (\boldsymbol{\tau}_t / \bar{\rho}) + \mathcal{G} \cdot \mathbf{u}_d''(\mathbf{x}_d, t) \right] \Delta t + H \Delta \mathbf{W}. \end{aligned} \quad (12)$$

The simplest closure for the second-order tensor \mathcal{G} is obtained through a simplified Langevin approach assuming isotropic turbulence, i.e., $\mathcal{G} = -\frac{1}{\delta\tau} \mathbf{I}$ where \mathbf{I} is the identity matrix. The sub-grid characteristic time scale $\delta\tau$ can be modeled as [4]

$$\delta\tau = \left(\frac{1}{2} + \frac{3C_0}{4} \right)^{-1} \frac{\delta k}{\delta\varepsilon}, \quad (13)$$

where the sub-grid turbulent kinetic energy and dissipation rate δk and $\delta\varepsilon$ can be approximated from the filtered velocity field in the framework of the Smagorinsky model [4] as

$$\delta k = 2C_Y \Delta^2 |S|^2, \quad (14a)$$

$$\delta\varepsilon = C_S \Delta^2 |S|^3. \quad (14b)$$

The Smagorinsky constant C_S and the Yoshizawa constant C_Y are taken to be 2.2×10^{-2} and 1.1×10^{-2} , respectively, following the suggestion in [4]; Δ is the cut-off scale, and $|S| = \sqrt{2S_{ij}S_{ij}}$ is the modulus of the filtered strain tensor calculated as

$$\mathbf{S} = \frac{1}{2} (\nabla \tilde{\mathbf{u}} + \nabla \tilde{\mathbf{u}}^T). \quad (15)$$

The Kolmogorov constant C_0 is conventionally taken to be 2.1; however, for the low Reynolds number flows we are considering, a somewhat lower value of 1.26 is used [4]. A parametric study is performed by using various values of C_0 including 2.1, 1.26 and 0.6 with a $32 \times 48 \times 32$ grid, and results are provided as Supplementary Material. No discernible differences were observed for different coefficients, hence the value of 1.26 is employed for the subsequent comparison. The insensitivity of SLM to the model parameter C_0 is partly attributed to the relatively coarse mesh that is employed, where the cut-off scale is in the middle of the inertia range and close to the integral scale. Turbulence in the counter-flow configuration is anisotropic [36]. With the inherent isotropic assumption, SLM is expected to only incompletely capture the anisotropic structure of the turbulence especially for coarse-grid simulations.

The last term on the right-hand side of Eq. (12) represents the Wiener process, which can be modeled as

$$H \Delta \mathbf{W} = \sqrt{C_0 \delta\varepsilon \Delta t} \boldsymbol{\xi}, \quad (16)$$

where the three components of $\boldsymbol{\xi}$ are independent standardized Gaussian random variables.

3. Conditions for spray-flame interactions to be significant

The study of various combustion modes for spray flames has been pioneered by Chiu and co-workers [37,38], and various regime diagrams for spray flames have been proposed [39]. Depending on the interspacing and the number density of the droplets, spray flames can be classified as external sheath combustion, external and internal group combustion, and single droplet combustion. More recently, regime diagrams for dilute spray conditions have been constructed to further distinguish between diffusion, premixed and partially premixed flames by introducing the equivalence ratio as an additional dimension [40]. The focus of the present study is on understanding the physical conditions under which flame-droplet interactions, and with this, dispersion becomes important, thereby requiring modeling.

Spray-flame interaction is primarily controlled by three competing physical processes: the transport of droplets, the rate of evaporation, and the existence of a flame. The droplet transport in physical space is determined by the underlying turbulent flow field, as well as the forces exerted on the droplet such as drag or lift. The rate of evaporation is affected by the heating rate provided by the ambient condition of the carrier phase, in addition to the thermo-physical properties of the droplet. Finally, the existence of a flame can be characterized by specific chemical time scales, such as the ignition delay and flame propagation time. To adequately describe these processes, relevant physical scales are derived and summarized in Table 1.

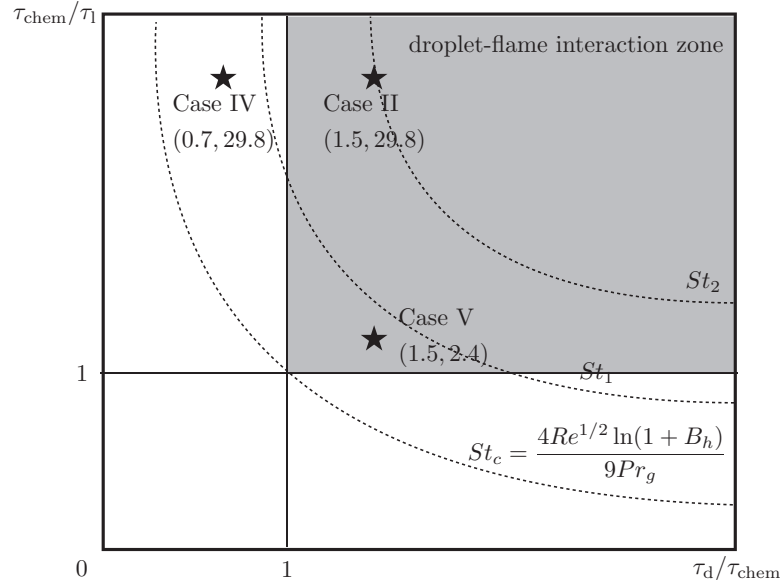


Fig. 2. Conditions for flame-droplet interactions to be important for models to capture. The three reacting cases are also located in the diagram, labeled by their respective values of the two time-scale ratios.

Table 1

Characteristic physical scales for spray-flame interactions. The description of the symbols and derivations are provided in the subsequent text.

Droplet relaxation time	$\tau_p = \frac{1}{18} \frac{\rho_l}{\rho_g} \frac{d_p^2}{\nu_g}$
Droplet life time	$\tau_d = \frac{9Pr_g}{4\ln(1+B_h)} \tau_p$
Chemical time scale	$\tau_{chem} = 1/\omega_c$
Velocity scale	U_d
Kolmogorov scales (time, length)	$\tau_\eta = (\nu/\varepsilon)^{1/2}$, $\eta = (\nu^3/\varepsilon)^{1/4}$
Integral scales (time, length)	$\tau_l = l/u'$, l

A prerequisite for significant flame-droplet interaction is the coexistence of the flame and droplet for a significant amount of time. This physical argument suggests two criteria: (i) the lifetime of a droplet (τ_d) should be longer than the characteristic chemical time scale (τ_{chem}); and (ii) the flame is thick enough to allow for sufficient interaction time. The first criterion can be described as $\tau_d \geq \tau_{chem}$, and a similar time scale ratio has been employed in [39,40] to distinguish between prevaporized spray flames and thick flames. The second criterion can be described by a Damköhler number that is defined using the integral time scale and the characteristic chemical time scale, i.e., $Da = \tau_l/\tau_{chem}$, and the requirement that $Da \leq 1$ (i.e., a more distributed flame as opposed to a thin flame). The two time-scale ratios, τ_d/τ_{chem} and τ_{chem}/τ_l , are used to construct the regime diagram shown in Fig. 2, where τ_{chem} is evaluated using the reaction rate ω_c for progress variable C . Consequently, the shaded area represents the parameter space where flame-droplet interaction is expected to be significant. For conditions outside the shaded region, effects of subgrid dispersion are insignificant because the contact time between droplets and the flame is negligible.

The point (1,1) in Fig. 2 represents a critical point that determines the onset of flame-droplet interaction. For a hyperbola that crosses this critical point, the following relation exists:

$$\left(\frac{\tau_d}{\tau_{chem}}\right) \times \left(\frac{\tau_{chem}}{\tau_l}\right) = \frac{\tau_d}{\tau_l} = 1. \quad (17)$$

Eq. (17) suggests the existence of a critical Stokes number, $St_{K,c}$ (i.e., $St_K = \tau_p/\tau_\eta$), because the droplet lifetime τ_d is related to the droplet relaxation time τ_p , and the integral time scale τ_l is related

to the Kolmogorov time scale τ_η through the Reynolds number. The formulation of this critical Stokes number is derived next.

To estimate the droplet lifetime, we consider the limiting case of the evaporation of a single droplet that is surrounded by a diffusion flame [41]

$$\tau_d = \frac{\rho_l d_p^2}{8\rho_g \alpha_g \ln(1+B_h)}, \quad (18)$$

where α_g is the thermal diffusivity of the gas phase. The Spalding heat transfer number B_h is calculated as

$$B_h = \frac{c_{p,m}(T_\infty - T_S)}{L_v}, \quad (19)$$

where T_∞ is taken to be the flame temperature, T_S is the surface temperature of the droplet and is assumed to be the boiling point temperature, and L_v is the latent heat of evaporation as defined in Section 2.2. Note that the relation in Eq. (19) is based on idealized conditions for a single droplet that is burning in quiescent air. The heat transfer number B_h is expected to be smaller when the droplets are in the regime of group combustion, where the majority of the droplets are enclosed by an external flame and the ambient temperature for an internal droplet could be cooler than the flame temperature. In that case, the lifetime of a single droplet τ_d is expected to be longer, which is favorable for the occurrence of flame-droplet interactions. For convective environments, additional correction factors for the Sherwood and Nusselt numbers have been introduced to improve the accuracy [42], which can reduce the lifetime of droplets. These details are ignored in the following derivation, as the purpose of Fig. 2 is to identify conditions that characterize the importance of spray-flame coupling.

Assuming that all properties are constant, τ_d is linearly related to the relaxation time scale τ_p through the following relation:

$$\tau_d = \frac{9Pr_g}{4\ln(1+B_h)} \tau_p. \quad (20)$$

A similar relation was derived in [40] through the analysis of mass transfer. There, the Schmidt number was employed instead of the Prandtl number and the Spalding mass transfer number B_m was employed instead of the Spalding heat transfer number B_h .

Table 2

Summary of the simulation configurations. The naming convention for each case follows the order of Reynolds number (Rxx), Stokes number (Sxx), and reaction conditions ('H' for hot, 'C' for cold).

Case	Reacting	d_p (μm)	Re_t	St_K
I (R200S16C)	No	80	200	16
II (R200S16H)	Yes	80	200	16
III (R200S01C)	No	20	200	1
IV (R200S01H)	Yes	20	200	1
V (R50S08H)	Yes	80	50	8

By invoking Kolmogorov's hypothesis [43], the Kolmogorov time scale can then be related to the integral time scale as

$$\tau_l = \tau_\eta Re_t^{1/2}, \quad (21)$$

where $Re_t = u'l/\nu$, based on the width of the injection slot $l = L$ and the fluctuating velocity u' . According to Eq. (17), by substituting τ_d and τ_l with Eqs. (18) and (21), the critical Stokes number is derived to be

$$St_{K,c} = \frac{4Re_t^{1/2} \ln(1 + B_h)}{9Pr_g}. \quad (22)$$

Based on these derivations, the dashed lines in Fig. 2 denote characteristic lines with constant Stokes numbers. Note that the flame-droplet interaction is only expected along a sub-section of the iso-Stokes-number lines.

It should be mentioned that the necessity and effectiveness of a dispersion model are tightly connected to the resolution of the grid. A time scale corresponding to the cut-off scale Δ can be defined as

$$\tau_\Delta = (\Delta^2/\delta\varepsilon)^{1/3}, \quad (23)$$

using the resolved-scale dissipation rate $\delta\varepsilon$ that is defined in Eq. (14b). Based on this time scale, a subgrid-scale Stokes number St_{SGS} can be defined and related to St_K as

$$St_{SGS} = \frac{\tau_p}{\tau_\Delta} \sim St_K(\eta/\Delta)^{2/3}. \quad (24)$$

In the DNS limit of $\eta/\Delta \sim 1$, no subgrid dispersion model is required because the flow field is well resolved by the grid. For a typical LES grid where $\eta/\Delta < 1$, St_{SGS} is expected to be smaller than St_K , and a subgrid dispersion model is needed to recover the influence of subgrid-scale stresses on the droplets. Eq. (24) shows that with decreasing ratio η/Δ , the droplets become more susceptible to the subgrid-scale fluctuations. In the case where a dispersion model is required and is expected to play a role, the flame-droplet interactions described in Fig. 2 add to the complexity of the sub-grid flow field, and modeling sub-grid dispersion becomes more challenging due to the presence of a flame.

Motivated by the regime diagram in Fig. 2 and the above discussion, three reacting conditions are identified for further investigation in this study. These conditions are listed in Table 2 and labeled in Fig. 2. The thermo-physical properties are evaluated based on the respective conditions obtained during the simulation. The cases with $St_K = 8$ and 16 are within the interactive zone, while the case with $St_K = 1$ lies outside the interactive zone, simply because the lifetime of the droplet is too short compared to the chemical time scale (i.e., $\tau_{chem}/\tau_d > 1$). More details on the computation and setup are provided in the next section.

4. Computational setup

Spray stagnation flames have been employed to study premixed and nonpremixed flame structures, chemical kinetics for liquid fuels, and extinction/ignition behaviors since 1960s [44]. In particular, experimental evidence shows the existence of double-flames,

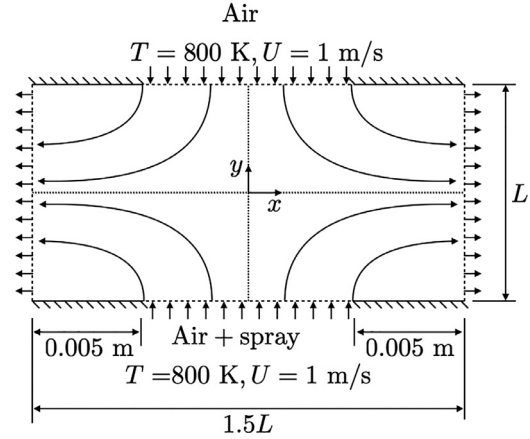


Fig. 3. A schematic of the simulation configuration.

consisting of a partially-premixed branch and a nonpremixed branch, when fuel spray is carried by air under fuel-rich conditions [45]. As such, this flame represents an ideal configuration to study spray-flame interactions. In this study, a three-dimensional counterflow turbulent spray flame is considered to examine the performance of the RDM dispersion model. The configuration features a turbulent counterflow with two opposed square slots at a separation distance of $L = 0.02$ m, as shown in Fig. 3. On the fuel side, which is at the bottom, pure air is injected with homogeneously distributed n-dodecane spray droplets at 800 K. The oxidizer side is composed of air at 800 K. Equal gas-phase mass flow rates from the fuel side and the oxidizer side are prescribed, with a mean velocity of 1 m/s. The flame is operated at atmospheric pressure. The global strain rate based on the mean air flow velocity is 100 1/s, and the overall equivalence ratio is 5.22. Based on the observations in [45], such conditions facilitate the creation of a double-flame structure. Additionally, the group number G_p , defined as $G_p = N_{tp}d_p/l_c$ [46], is computed to be approximately 19 for Cases II and V, and 311 for Case IV, based on the total number of droplets N_{tp} within a characteristic length scale l_c that is taken to be the streamwise domain length before the stagnation plane (i.e., $l_c = 0.75L$). Therefore, all the reacting conditions fall in the group combustion regime where the point droplet assumption is valid, as indicated in Section 2.2. The volume fraction of the droplets for all cases is approximately 3.3×10^{-4} , placing the spray in the dilute suspension regime according to [47] so that droplet-droplet interactions can be ignored.

A turbulent velocity profile is prescribed at the fuel side by superimposing a synthetic turbulence field over the mean injection velocity following Taylor's hypothesis. Two turbulence levels are considered, corresponding to turbulent Reynolds numbers of $Re_t = 50$ and 200. The liquid fuel is injected by monodispersed droplets. Two representative spray initial droplet diameters d_p are considered in this study, namely $d_p = 20 \mu\text{m}$ and $d_p = 80 \mu\text{m}$, corresponding to $St_K = 1$ and 16 for $Re_t = 200$, respectively. The initial velocity for the droplets is set to be the same as their underlying carrier phase velocity. Neumann boundary conditions are imposed on the outlet.

Droplets with a diameter of 80 μm are expected to cross the stagnation plane, such that the spray is not fully evaporated before reaching the flame, which provides suitable conditions for studying the influence of combustion on the dispersed-phase sub-grid models. Based on the injection velocity U_j , it takes a fluid parcel approximately $\tau_l = L/(2U_j) = 10$ ms to reach the stagnation plane.

By changing Re_t and St_K , as summarized in Table 2, the effects of droplet dispersion, evaporation, and turbulence on the flame structure are examined. It should be noted that for all reacting

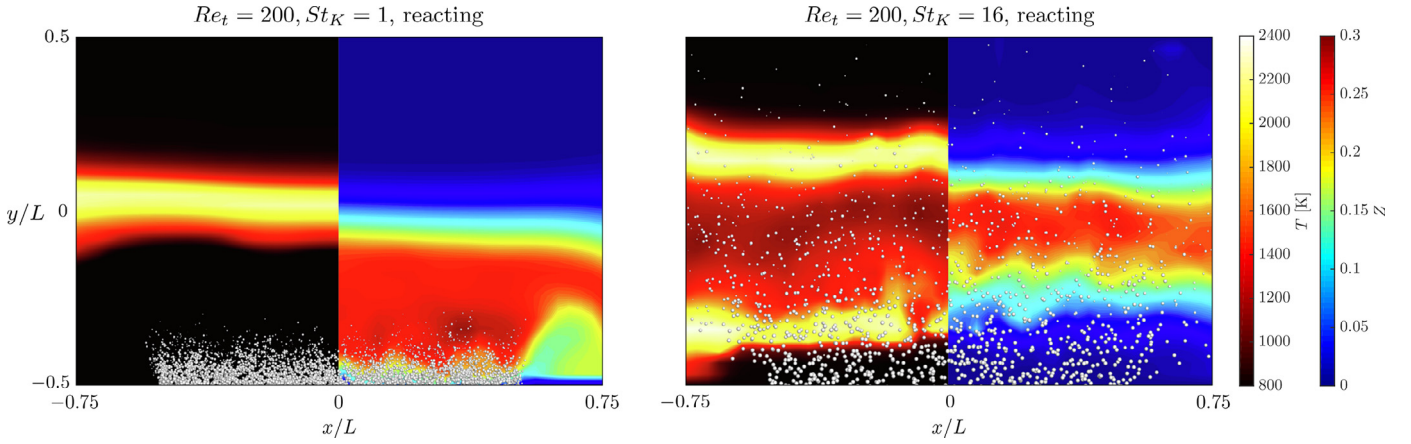


Fig. 4. Instantaneous temperature field for Case R200S01H (left) and Case R200S16H (right). Droplets are represented by white scatters in both figures. The white contour corresponds to the line of stoichiometry.

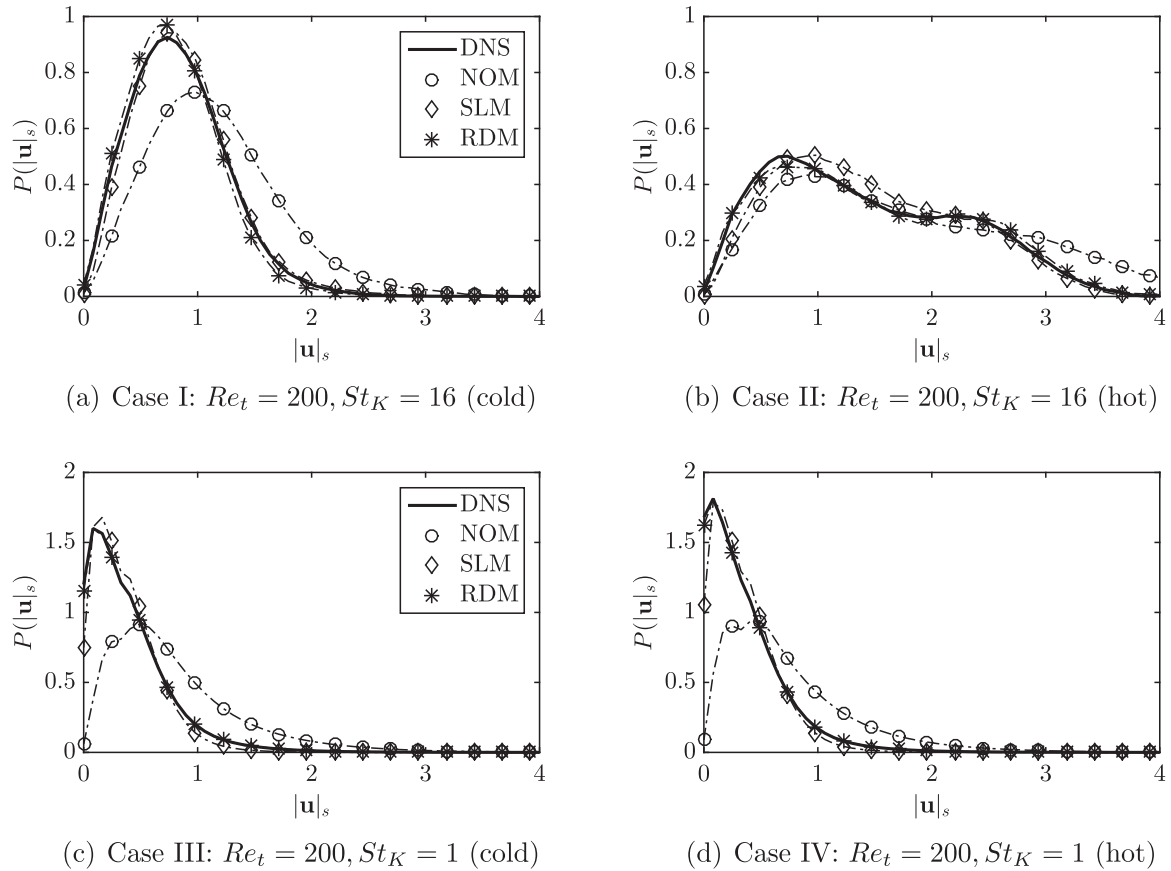


Fig. 5. PDF of droplet slip velocity obtained from *a priori* analysis for $St_K = 1$ and 16, under inert and reacting conditions for (a) Case I: $Re_t = 200$, $St_K = 16$ (cold), (b) Case II: $Re_t = 200$, $St_K = 16$ (hot), (c) Case III: $Re_t = 200$, $St_K = 1$ (cold), and (d) Case IV: $Re_t = 200$, $St_K = 1$ (hot).

simulations, the FPV model, described in Section 2, is used to account for the effect of chemical reactions. For each of the five cases listed in Table 2, four simulations are performed, including DNS, LES without any dispersion model (NOM), LES using a simplified Langevin model (SLM), and LES using RDM that is developed here. The DNS was conducted with a uniform mesh of $128 \times 192 \times 128$ grid points. Two sets of LES are conducted, with successively coarser grids. The finer LES (LES-F) employs a dynamic Smagorinsky closure on a $64 \times 96 \times 64$ grid, while the coarser simulation (LES-C) employs a $32 \times 48 \times 32$ grid. The cut-off scales for both meshes reside within the inertial range of the turbulence kinetic energy spectrum of the inflow turbulence, and a further re-

duction of the grid size pushes the cut-off scale to be in the neighborhood of the integral scale.

5. Results and discussion

5.1. *A priori* analysis

To avoid the complication of cumulative errors, an *a priori* analysis of the slip velocity $\mathbf{u}_s = \mathbf{u}^+ - \mathbf{u}_d$ is first conducted. The slip velocity is employed in the evaluation of the drag force, hence it directly impacts the droplet dynamics and the two-way coupling between the gas and droplet phases. DNS of all five cases listed

in Table 2 are first performed. As an example, Fig. 4 shows the instantaneous mixture fraction and temperature contours for the Cases R200S01H and R200S16H. The slip velocity is then evaluated and averaged over the whole computational domain, and an explicit box filter with homogeneous filter width $\Delta_f = 8\Delta_{DNS}$ is applied to the DNS field to obtain the filtered quantities that are required by the models. It is noted that two distinctively different flame structures are observed for Case R200S01H ($St_K = 1$) and for Case R200S16H ($St_K = 16$). As shown in Fig. 4, all droplets are evaporated before they reach the flame for Case R200S01H, hence there is no spray-flame interaction in this case and the spray dynamics is expected to be similar between the inert and reacting cases. The flame is similar to a gas-phase counterflow diffusion flame. In contrast, double-flames are observed for Case R200S16H and Case R50S08H (not shown), where the first flame (fuel-side) is a partially premixed flame and the second flame (oxidizer-side) is a diffusion flame [17]. The majority of the droplets interact with the first flame and continue to evaporate to form the second flame. PDFs of the slip velocity are compared between DNS and the three models in Fig. 5, for the first four cases listed in Table 2, as Case R50S08H behaves similarly to Case R200S16H. For both the inert and reacting DNS with $St_K = 1$ (Figs. 5(c) and 5(d)) the peak of the PDF is close to zero, which confirms that the slip velocity is low in flows with small St_K . Droplets in this situation follow the carrier flow closely. For the case with $St_K = 16$ (Figs. 5(a) and 5(b)), the peak of the PDF migrates to a larger value (~ 1 m/s), because the droplets are less responsive to the dynamics of the carrier flow field at higher St_K .

In addition to the Stokes number, another factor that influences the droplet dynamics is combustion. Note that there is no significant difference between the inert (Fig. 5(c)) and reacting

cases (Fig. 5(d)) for $St_K = 1$ because the droplets complete evaporation before interacting with the flame. In contrast, for $St_K = 16$, the spreading of $P(|\mathbf{u}_s|)$ is larger for the reacting case compared to the inert case, as shown in Figs. 5(a) and 5(b). Recall that a double-flame structure is observed in Fig. 4 for Case R200S16H, where droplets penetrate through the partially premixed flame and evaporation proceeds, providing fuel vapor to support the secondary flame. Flame-induced dilatation, particularly in the partially premixed flame, causes an increase in droplet slip velocity. As illustrated in Fig. 2, the different responses of Cases R200S01H and R200S16H reflect mainly their different droplet lifetime.

By comparing results between dispersion models and DNS, it is observed that the discrepancy is more significant for flows with small St_K , where the slip velocity closely resembles the magnitude of the sub-grid fluctuations. There, ignoring the sub-grid dispersion leads to over-predictions of the droplet slip velocity (e.g., LES-NOM). Both RDM and SLM provide improved predictions of \mathbf{u}_s , which are in good agreement with DNS. With increasing St_K , the trajectories of the droplets deviate from the instantaneous flow field due to increasing impact of the inertia. In this case, the benefit of recovering the sub-grid velocity fluctuations is less significant compared to that for smaller droplets. As a consequence, discrepancies among different modeling approaches are smaller for cases with $St_K > 1$ compared to those with $St_K \leq 1$. For the case R200S16H, RDM shows better agreement with the DNS results near the peak, compared to SLM and NOM.

It should be pointed out that the *a priori* analysis collects statistics by evaluating the slip-velocity formulation from explicitly filtering DNS. When cumulative effects and other modeling errors are introduced, as is discussed next in Section 5.2, the responses of the

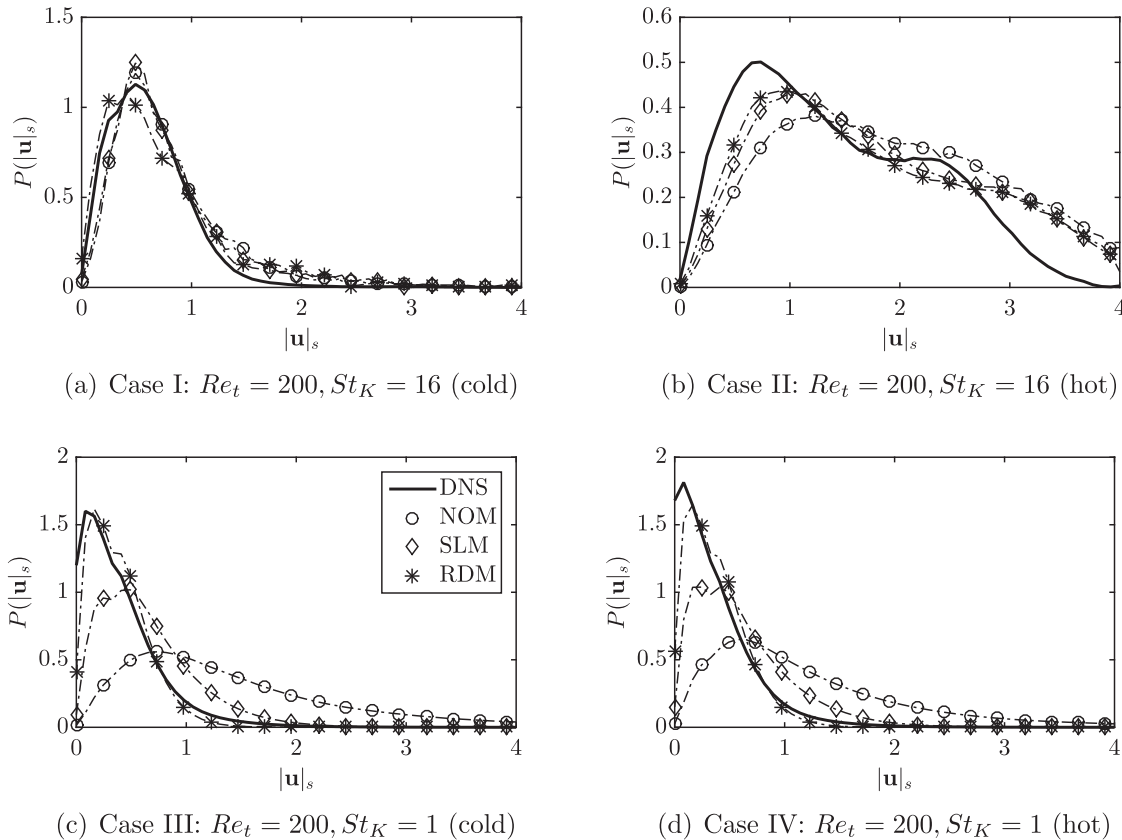


Fig. 6. PDF of droplet slip velocity obtained from *a posteriori* LES for $St_K = 1$ and 16, under inert and reacting conditions for (a) Case I: $Re_t = 200, St_K = 16$ (cold), (b) Case II: $Re_t = 200, St_K = 16$ (hot), (c) Case III: $Re_t = 200, St_K = 1$ (cold), and (d) Case IV: $Re_t = 200, St_K = 1$ (hot) using the LES-C grid ($4\Delta_{DNS}$).

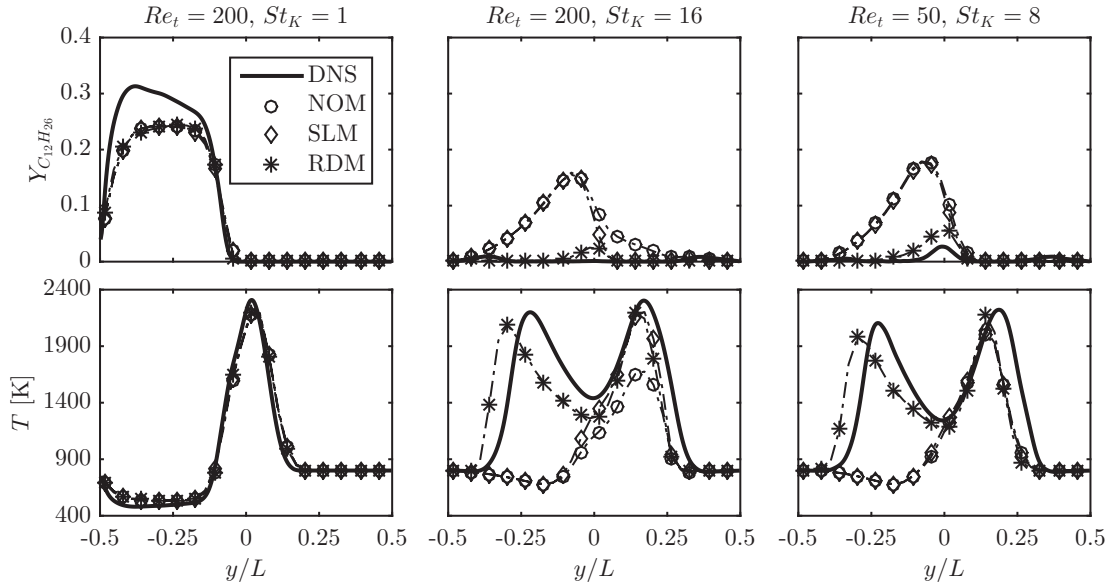


Fig. 7. Mean profiles of $Y_{C_{12}H_{26}}$ and temperature in the streamwise direction for R200S01H (left), R200S16H (middle), and R50S08H (right) using the LES-C grid ($4\Delta_{DNS}$).

models might be different from what is observed in this section. In addition, although SLM and RDM are effective in recovering the sub-grid scale motion in the *a priori* analysis, the overall impact on the flame characteristics is possible to be negligible for $St_K = 1$, due to the short droplet lifetime as shown in Fig. 2. On the contrary, for $St_K > 1$, although the differences between models per time step are minor, the impact on the flame structure can be cumulative considering the long droplet lifetime.

5.2. A posteriori simulations

In this section, we consider the sub-grid influence on the dispersed phase by applying the models that were introduced in Section 2 to LES of the counterflow spray flame. The performance of the models is analyzed for both inert and reacting conditions listed in Table 2.

5.2.1. Impact of the sub-grid dispersion on velocity and scalar fields

Figure 6 shows $P(|\mathbf{u}_s|)$ from the LES with different modeling approaches. For $St_K = 1$, the slip velocity is significantly over-predicted without a sub-grid dispersion model. Deterioration in the prediction of \mathbf{u}_s is observed with SLM, while good agreement between RDM and DNS is maintained in both the *a priori* and *a posteriori* tests. The disagreement between SLM and DNS can possibly be attributed to the specification of a single turbulence time scale that is modeled using resolved turbulent kinetic energy and turbulent dissipation rate in SLM. In addition, turbulence in the counterflow configuration is anisotropic with axisymmetric two-dimensional characteristics, as demonstrated in [36]. The SLM model assumes isotropic turbulence for the sub-grid scale, hence cannot recover the correct turbulence structure especially when the grid is coarse compared to DNS. In contrast, no assumption about the nature of turbulence is made in RDM; it directly improves the prediction near the cut-off scale, which can be particularly effective for the target flame. To further understand the impact of the dispersion models on combustion, we show the mean profiles for fuel mass fraction $Y_{C_{12}H_{26}}$ and temperature in Fig. 7. No distinguishable differences in temperature are observed for Case R200S01H between the results from LES with different modeling approaches and the DNS. The fuel mass fraction close to the inlet ($y/L = -0.5$) is under-predicted by all modeling approaches, which suggests that the rate of evaporation is under-predicted in LES.

Note that fuel droplets are fully evaporated before reaching the flame in Case R200S01H. The spray flame is in the pre-vaporized regime, as defined in Fig. 2, so that the short droplet lifetime results in an insensitive model responses.

In contrast to Case R200S01H, the cases where $St_K = 8$ and $St_K = 16$ exhibit significantly different behaviors in the scalar fields between LES and DNS, as shown in Fig. 7. Recall that Fig. 4 shows that droplets cross the stagnation plane, and the formation of a double-flame structure is observed. The double-flame structure is not captured by the LES where the contribution of sub-grid dispersion is insufficiently captured, as shown by the NOM and SLM results in Fig. 8, and only the diffusion flame on the oxidizer side is formed. As a consequence, the fuel mass fraction is over-predicted on the fuel side, which is confirmed in Fig. 7. With the consideration of sub-grid dispersion effects in RDM, the double-flame structure for Cases R200S16H and R50S08H is recovered. Note that the peak temperature of the flame on the oxidizer side in Fig. 7 shows better agreement between DNS and LES of Case R50S08H compared to Case R200S16H. This difference is a manifestation of the turbulence-flame interaction. For the case with a smaller Reynolds number, hence smaller sub-grid fluctuation, the errors due to the turbulent combustion models are less significant.

When a finer mesh is employed in the LES (i.e., LES-F with $2\Delta_{DNS}$), all three models can recover the double-flame structure, as demonstrated by the temperature and fuel mass fraction profiles in Fig. 9 for the Case R200S16H. Turbulence fluctuations are better resolved by the grid, and even NOM can correctly predict the flame structure. Comparing the results obtained from the coarse and fine LES grids, it can be observed that recovering the sub-grid dispersion can have a direct impact on the prediction of flame structure, and RDM has a wider range of applicability in terms of mesh resolution compared to the other two models. Since no distinct differences are observed for the well-resolved LES, the subsequent analysis is applied to the coarse-grid LES only.

5.2.2. Dynamic interactions between droplets and carrier flow

The differences in flame topology, as a result of sub-grid dispersion models, are found to be caused by turbulence modulation through the two-way mass, momentum and energy coupling. To investigate the impact of the dispersed phase on the turbulence fluctuation, we show statistics related to the dispersed phase in Fig. 10, where the streamwise profiles for droplet number density

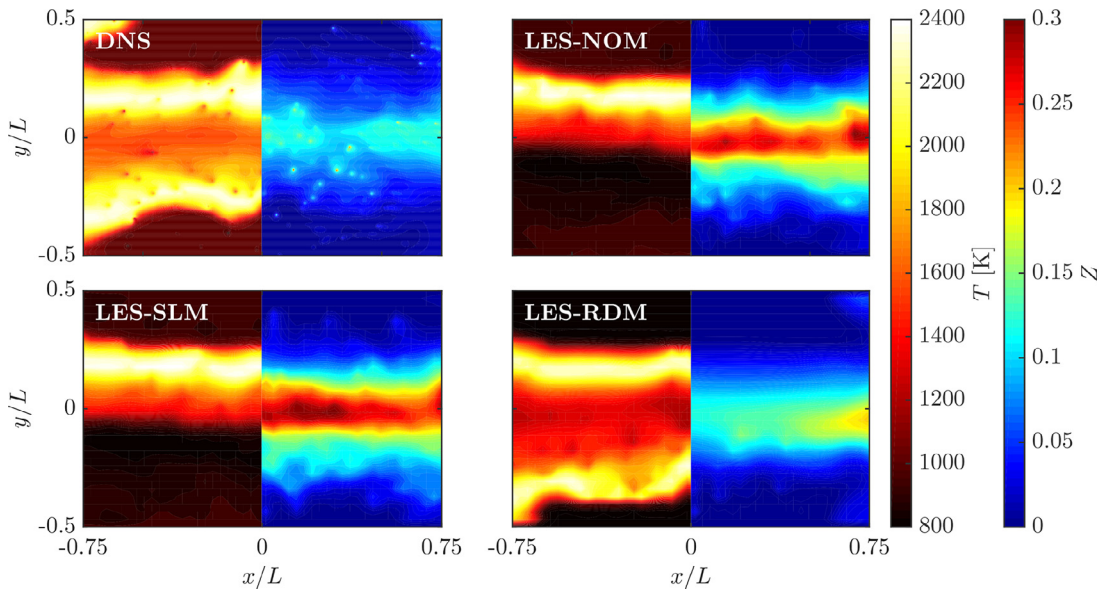


Fig. 8. Instantaneous mixture fraction and temperature field upon the onset of ignition of the fuel-side flame for case R200S16 using the LES-C grid ($4\Delta_{DNS}$).

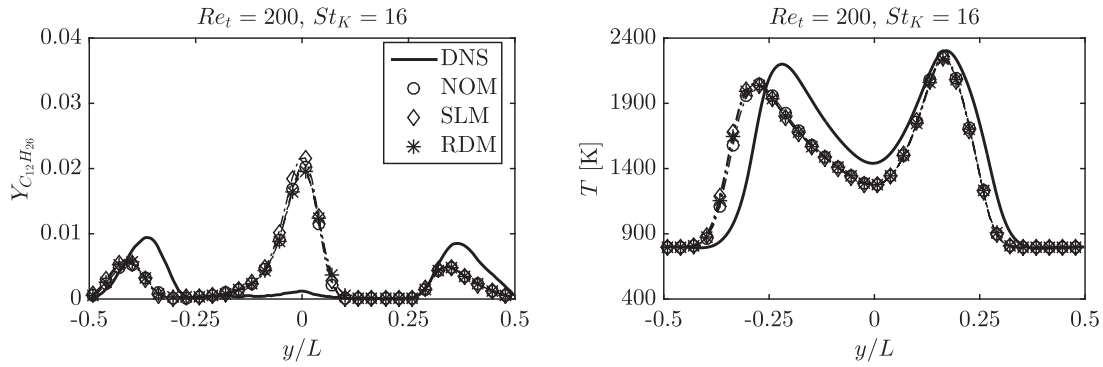


Fig. 9. Mean profiles of $Y_{C_{12}H_{26}}$ and temperature in the streamwise direction for R200S16H using LES-F grid ($2\Delta_{DNS}$).

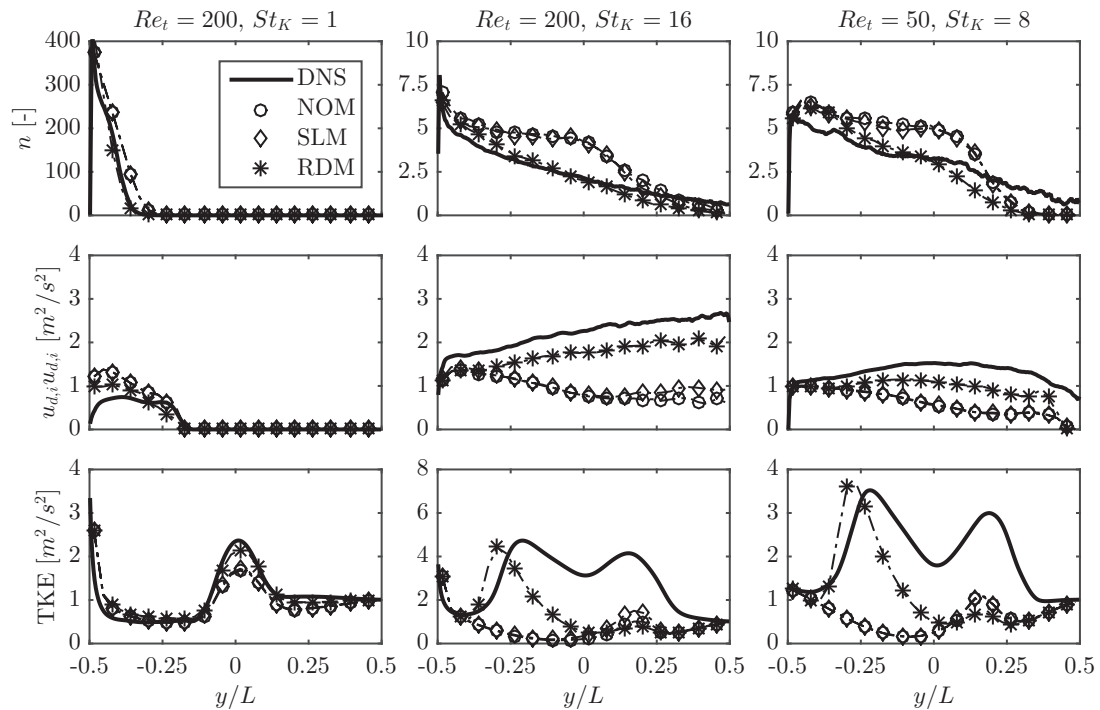


Fig. 10. Mean number density, turbulent kinetic energy profiles of the dispersed phase and turbulent kinetic energy profiles of the carrier phase in the streamwise direction for cases R200S01H, R200S16H, and R50S08H using the LES-C grid ($4\Delta_{DNS}$).

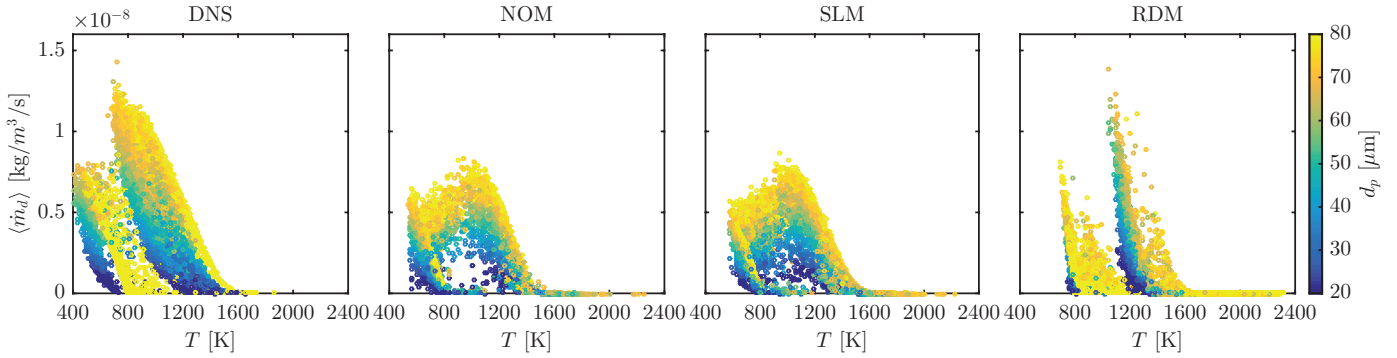


Fig. 11. Scatter plots of instantaneous evaporation source term for cases R200S16H, colored by droplet diameter, obtained using the LES-C grid ($4\Delta_{\text{DNS}}$).

(n), the variance of the droplet velocity $u_{d,i}u_{d,i}$, and the gas-phase turbulent kinetic energy (TKE) for different modeling approaches are compared with DNS. Due to the heat release from the partially-premixed flame, the droplet number density decays at a constant rate in the DNS and in LES-RDM. For cases with NOM and SLM, the absence of the flame leads to an under-prediction of the droplet evaporation. As a consequence, the droplet number density is over-predicted from $y/L = -0.5$ to $y/L = 0$. In LES-NOM, a decay of $u_{d,i}u_{d,i}$ along the streamwise direction is observed for both Cases R200S16H and R50S08H. A similar behavior is observed for LES-SLM, where a slight increase in $u_{d,i}u_{d,i}$ is observed at $y/L = 0.25$ for the Case R200S16H. This leads to the improved prediction of the peak temperature in Fig. 7. Reasonably good agreement with the DNS results is observed with LES-RDM, which indicates an improved representation of the droplet motion by LES-RDM.

As a consequence of the improved prediction of the dispersed phase, the prediction of the carrier phase is also improved, due to the consideration of two-way coupling. As reflected in the gas-phase turbulent kinetic energy, shown in Fig. 10, LES-RDM predicts comparable levels of carrier-phase TKE as DNS near the partially premixed flame, whereas LES-NOM and LES-SLM both under-predict the turbulence for Cases R200S16H and R200S08H. The scatter plot comparing the evaporation source term in Fig. 11 further shows that the evaporation rates are also better predicted by RDM in terms of magnitude and correlation with droplet diameters. This is because the evaporation source term is a function of the ambient temperature and fuel mass fraction that are determined by the droplet locations. The modifications in the carrier-phase velocity and scalar fields eventually lead to the appropriate representation of the double-flame structures in the LES-RDM model. Note that $u_{d,i}u_{d,i}$ in Case R50S08H is lower than in Case R200S16H, as a result of the reduced Reynolds number of the carrier flow. In contrast to the observed differences for Cases R200S16H and R50S08H, the statistical profiles are comparable for Case R200S01H for all modeling approaches due to the insignificant flame-droplet interactions as described by the regime diagram in Fig. 2, which is consistent with the prediction from Fig. 7.

6. Conclusions

In this study, a deconvolution based sub-grid dispersion model is developed to account for the impact of sub-grid momentum and scalar fluctuations on spray droplets. The performance of sub-grid dispersion models under combustion conditions is studied through *a priori* and *a posteriori* analyses of a counterflow turbulent n-dodecane spray flame. Three conditions with different Reynolds numbers and droplet diameters are investigated, covering the limits of small and large Stokes numbers. The deconvolution-based sub-grid dispersion model is constructed for velocity and scalars. Two other popular closure models, namely a simplified Langevin

model and a “dispersion-free” model, are also examined, and the performance of these models is compared.

To understand the physical conditions that lead to strong flame-droplet interactions, a regime diagram is constructed. Based on the proposition, appreciable turbulence/spray interaction requires the following conditions:

- The lifetime of droplets has to be sufficiently long to enable the interaction with the flame, which is represented as $\tau_d/\tau_{\text{chem}} > 1$;
- The flame has to be sufficiently thick to allow for sufficient contact time between droplets and flame, which requires $1/Da = \tau_{\text{chem}}/\tau_l > 1$.

The regime diagram clearly shows that spray-flame interactions require consideration for the test cases with large Stokes number. The tendency of spray-flame interactions is enhanced when spray droplets exhibit group combustion behavior as in the test cases studied here.

Both *a priori* and *a posteriori* analyses are conducted to test the performance of the different modeling approaches for the sub-grid dispersion, for both inert and reacting conditions. Through *a priori* analysis, it is shown that RDM and SLM consistently outperform NOM in predicting the slip velocity, and differences between the models are more significant at smaller Stokes numbers. In the *a posteriori* analyses, the differences in slip velocities between various LES models and DNS are insignificant for smaller Stokes numbers, because of the relatively short droplet lifetime under these conditions. For droplets with large Stokes numbers, qualitative differences are observed in the flame topology; a double-flame structure is predicted in DNS and is captured by LES-RDM, however, the fuel-side flame is not captured in LES-NOM and LES-SLM because these models cannot capture the nonlinear interactions between evaporation, turbulence, and heat transfer. LES-RDM is shown to recover the sub-grid statistics of the droplets, hence modify the turbulent kinetic energy of the carrier-phase through two-way coupling. When the LES mesh is refined, all three models can capture the double-flame structures. For the flames examined in this work, the proposed RDM model can provide an improved and more robust closure to sub-grid dispersion when flames are present compared to the other two models. Future work includes extension of the RDM closure to application with unstructured meshes, as well as to combustion conditions at higher turbulence intensities.

Acknowledgment

Financial support through NASA with award #NNX15AV04A is gratefully acknowledged. Resources supporting this work were provided by the NASA High-End Computing (HEC) Program through

the NASA Advanced Supercomputing (NAS) Division at Ames Research Center. X. Zhao is grateful for the financial support from the Center for Turbulence Research Summer Program (2016) to start this investigation.

Supplementary material

Supplementary material associated with this article can be found, in the online version, at doi: [10.1016/j.combustflame.2019.05.032](https://doi.org/10.1016/j.combustflame.2019.05.032)

References

- [1] J.-P. Minier, S. Chibbaro, S.B. Pope, Guidelines for the formulation of Lagrangian stochastic models for particle simulations of single-phase and dispersed two-phase turbulent flows, *Phys. Fluids* 26 (2014) 113303.
- [2] A.D. Gosman, E. Loannides, Aspects of computer simulation of liquid-fueled combustors, *J. Energy* 7 (2012) 482–490.
- [3] M. Bini, W.P. Jones, Large-eddy simulation of particle-laden turbulent flows, *J. Fluid Mech.* 614 (2008) 207–252.
- [4] P. Fede, O. Simonin, P. Villedieu, K.D. Squires, Stochastic modeling of the turbulent subgrid fluid velocity along inertial particle trajectories, *CTR Summer Program* (2016), pp. 247–258.
- [5] A.S. Berrouk, D. Laurence, J.J. Riley, D.E. Stock, Stochastic modeling of inertial particle dispersion by subgrid motion for LES of high Reynolds number pipe flow, *J. Turbul.* 8 (2007) N50.
- [6] G. Jin, G.-W. He, A nonlinear model for the subgrid timescale experienced by heavy particles in large eddy simulation of isotropic turbulence with a stochastic differential equation, *New J. Phys.* 15 (2013) 035011.
- [7] J. Pozorski, S.V. Apte, Filtered particle tracking in isotropic turbulence and stochastic modeling of subgrid-scale dispersion, *Int. J. Multiph. Flow* 35 (2009) 118–128.
- [8] B. Shotorban, F. Mashayek, Modeling subgrid-scale effects on particles by approximate deconvolution, *Phys. Fluids* 17 (2005) 081701.
- [9] J.G.M. Kuerten, Subgrid modeling in particle-laden channel flow, *Phys. Fluids* 18 (2) (2006) 025108.
- [10] W.R. Michalek, J.G.M. Kuerten, J.C.H. Zeegers, R. Liew, J. Pozorski, B.J. Geurts, A hybrid stochastic-deconvolution model for large-eddy simulation of particle-laden flow, *Phys. Fluids* 25 (2013) 123302.
- [11] B. Ray, L.R. Collins, A subgrid model for clustering of high-inertia particles in large-eddy simulations of turbulence, *J. Turbul.* 15 (2014) 366–385.
- [12] M.J. Cernick, S.W. Tullis, M.F. Lightstone, Particle subgrid scale modelling in large-eddy simulations of particle-laden turbulence, *J. Turbul.* 16 (2014) 101–135.
- [13] J.M. MacInnes, F.V. Bracco, Stochastic particle dispersion modeling and the tracer-particle limit, *Phys. Fluids A* 4 (1992) 2809–2824.
- [14] B. Naud, Particle dispersion modeling based on the generalised Langevin model for the seen velocity, *Seventh international symposium on turbulence, heat and mass transfer* (2012), pp. 853–862.
- [15] B. Shotorban, F. Mashayek, A stochastic model for particle motion in large-eddy simulation, *J. Turbul.* 7 (2006) N18.
- [16] M. Ihme, H. Pitsch, Modeling of radiation and nitric oxide formation in turbulent nonpremixed flames using a flamelet/progress variable formulation, *Phys. Fluids* 20 (2008) 055110.
- [17] A. Vié, B. Franzelli, Y. Gao, T. Lu, H. Wang, M. Ihme, Analysis of segregation and bifurcation in turbulent spray flames: A 3D counterflow configuration, *Proc. Combust. Inst.* 35 (2) (2015) 1675–1683.
- [18] P. Jenny, D. Roekaerts, N. Beishuizen, Modeling of turbulent dilute spray combustion, *Prog. Energy Combust. Sci.* 38 (2012) 846–887.
- [19] G. Continillo, W. Sirignano, Counterflow spray combustion modeling, *Combust. Flame* 81 (1990) 325–340.
- [20] M. Germano, U. Piomelli, P. Moin, W.H. Cabot, A dynamic subgrid-scale eddy viscosity model, *Phys. Fluids* 3 (1991) 1760–1765.
- [21] C.D. Pierce, P. Moin, Progress-variable approach for large-eddy simulation of non-premixed turbulent combustion, *J. Fluid Mech.* 504 (2004) 79–97.
- [22] M. Ihme, L. Shunn, J. Zhang, Regularization of reaction progress variable for application to flamelet-based combustion models, *J. Comput. Phys.* 231 (2012) 7715–7721.
- [23] M. Ihme, H. Pitsch, Prediction of extinction and reignition in nonpremixed turbulent flames using a flamelet/progress variable model. 2. Application in LES of Sandia flames D and E, *Combust. Flame* 155 (1–2) (2008) 90–107.
- [24] Q. Wang, T. Jaravel, M. Ihme, Assessment of spray combustion models in large-eddy simulations of a polydispersed acetone spray flame, *Proc. Combust. Inst.* 37 (2019) 3335–3344.
- [25] E. Gutheil, W.A. Sirignano, Counterflow spray combustion modeling with detailed transport and detailed chemistry, *Combust. Flame* 113 (1998) 92–105.
- [26] H. Olguin, E. Gutheil, Theoretical and numerical study of evaporation effects in spray flamelet modeling, *ERCOTAC Series*, 19, Springer (2014), pp. 79–106.
- [27] B. Franzelli, B. Fiorina, N. Darabiha, A tabulated chemistry method for spray combustion, *Proc. Combust. Inst.* 34 (2013) 1659–1666.
- [28] B. Franzelli, A. Vié, M. Ihme, On the generalisation of the mixture fraction to a monotonic mixing-describing variable for the flamelet formulation of spray flames, *Combust. Theor. Model.* 19 (6) (2015) 773–806.
- [29] R.S. Miller, J. Bellan, Direct numerical simulation and subgrid analysis of a transitional droplet laden mixing layer, *Phys. Fluids* 12 (2000) 650.
- [30] W.E. Ranz, W.R. Marshall Jr., Evaporation from drops, Part I, *Chem. Eng. Prog.* 48 (3) (1952) 141–146.
- [31] C.T. Crowe, M.P. Sharma, D.E. Stock, The particle-source-in cell (PSI-CELL) model for gas-droplet flows, *J. Fluids Eng.* 99 (2) (1977) 325–332.
- [32] Q. Wang, M. Ihme, Regularized deconvolution method for turbulent combustion modeling, *Combust. Flame* 176 (2017) 125–142.
- [33] J.W. Labahn, C.B. Devaud, T.A. Sipkens, K.J. Daun, Inverse analysis and regularisation in conditional source-term estimation modelling, *Combust. Theor. Model.* 18 (2014) 474–499.
- [34] A.W. Cook, Determination of the constant coefficient in scale similarity models of turbulence, *Phys. Fluids* 9 (5) (1997) 1485–1487.
- [35] Q. Wang, M. Ihme, A regularized deconvolution method for turbulent closure modeling in implicitly filtered large-eddy simulation, *Combust. Flame* 204 (2019) 341–355.
- [36] S. Lyra, H. Kolla, B. Coriton, A. Gomez, J.H. Frank, J.H. Chen, Counterflow H₂/air premixed flames under intense turbulence and strain, *8th U. S. National Combustion Meeting*, Park City, UT (2013), pp. 1–6.
- [37] T. Suzuki, H.H. Chiu, Multi-droplet combustion of liquid propellants, *9th International Symposium of Space Technological Sciences* (1971), pp. 145–154.
- [38] H.H. Chiu, T.M. Liu, Group combustion of liquid droplets, *Combust. Sci. Tech.* 17 (1977) 127–142.
- [39] R. Borghi, Background on droplets and sprays, *Combustion and Turbulence in Two-phase Flows*, Lecture series 1996-02, Von Karman Institute for Fluid Dynamics, 1996.
- [40] J. Revelillon, L. Vervisch, Analysis of weakly turbulent dilute-spray flames and spray combustion regimes, *J. Fluid Mech.* 537 (2005) 317–347.
- [41] S. Turns, *An introduction to combustion: concepts and applications*, McGraw-Hill, 2000.
- [42] K.K. Kuo, *Principles of combustion*, Wiley, 1986.
- [43] S. Pope, *Turbulent flows*, Cambridge University Press, 2000.
- [44] S.C. Li, Spray stagnation flames, *Prog. Energy Combust. Sci.* 23 (1997) 303–347.
- [45] S.C. Li, F.A. Williams, Experimental and numerical studies of two-stage methanol flames, *Proc. Combust. Inst.* 26 (1996) 1024–1074.
- [46] C.K. Law, *Combustion physics*, Cambridge University Press, 2006.
- [47] S. Elghobashi, On predicting particle-laden turbulent flows, *Appl. Sci. Res.* 52 (1994) 309–329.